ACS APPLIED ENERGY MATERIALS
Cite This: ACS Appl. Energy Mater. 2019, 2, 2862−2869
Article
www.acsaem.org

Nickel-Ion-Oriented Fabrication of Spiny PtCu Alloy Octahedral Nanoframes with Enhanced Electrocatalytic Performance

Guilin Zhu,[†] Jiawei Liu,[†] Shuo Li, Yunpeng Zuo, Dian Li, and Heyou Han*

State Key Laboratory of Agricultural Microbiology, College of Science, Huazhong Agricultural University, No. 1, Shizishan Street, Hongshan District, Wuhan 430070, P. R. China

Supporting Information

ABSTRACT: Metal cation is an emerging type of morphology controlling agency in nanoscience, but has rarely been used in fabrication of hollow structures. Herein, with the addition of Ni^{2+} ion, PtCu alloy octahedral nanoframes (PtCu AONFs) with plenty of spiny nanothorns on the apexes are synthesized via one-step hydrothermal reaction. Ni^{2+} ion plays a pivotal role in forming hollow structures because it facilitates the diffusion of Cu atoms in the replacement reaction between initially formed Cu templates and $PtCl_6^{2-}$. The as-prepared PtCu AONFs show a superior electrocatalytical activity and durability toward oxygen reduction reaction (ORR) with a mass activity (MA) and specific activity (SA) of 0.28 A/mg_{Pt} and 0.50 mA/cm^2 at 0.90 V vs reversible hydrogen electrode (RHE), which are 2.8- and 2.6-fold times that of commercial Pt/C (0.10 A/mg_{Pt} and 0.19 mA/cm^2). In addition, the electrocatalytical oxidation property of PtCu AONFs toward methanol also better than that of commercial Pt/C. This study offers a new strategy for synthesizing hollow electrocatalysts with enhanced properties.

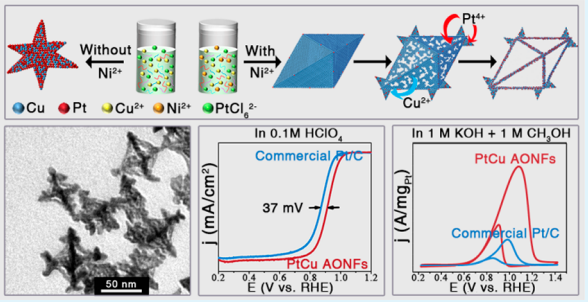

KEYWORDS: *metal cation, PtCu nanoframes, spiny nanothorns, oxygen reduction reaction, methanol oxidation reaction*

1. INTRODUCTION

Among the numerous energy technologies, proton exchange membrane fuel cells (PEMFCs) are generally acknowledged as one of the most promising devices because they meet almost all the expectations of future energy prospects such as being renewable, environmentally friendly, and sustainable.[1−9] Although Pt is publicly recognized as the most active metallic catalyst for PEMFCs, its energy conversion efficiency is still limited by commercial Pt/C because of the poor catalytic performance and high price.[4−6] Two effective methods to increase the electrocatalytic performance of Pt-based catalysts are changing the surface electronic structure and increasing the specific surface area.[10−18] Alloying Pt with other transition metals is a common approach to change the surface electronic structure of the catalytic metal, such as $PtCo_3$ NPs,[19] PtCu NCs,[20−23] Pt−Ni/Ni-B composite.[24]

Although the increase in specific surface area often realized by regulating the morphology of nanomaterials, whose interface between reaction molecules and catalyst can be largely increased, and the efficiency of electrocatalytic reaction can be enhanced.[10,13] In traditional methods, organic surfactants were utilized to control the morphology due to their selective binding effect on different facets.[10,25−27] For example, CTAB played a pivotal role in fabricating porous Pt nanotubes and cubic $PtCu_3$ nanocages;[22,28,29] Pluronic F127 was crucial for the synthesis of porous Au@Pd@Pt nanospheres;[30] and PVP assisted the formation of Pd−Pt core−shell polyhedron.[31,32] Octadecylamine (ODA) facilitated the fabrication of Au−Ag octahedral NFs.[33] Among various kinds of nanocrystal morphologies, hollow NFs are a class of highly promising and competitive nanostructures in electrocatalysis because of their unique omnidirectional exposed ridges skeletons, which can remarkably maximize the utilization efficiency of Pt to achieve cost savings.[34−38] However, the fabrication processes of these NFs always need multiple steps, increasing the difficulty in operation.[35]

Recently, some metal ions, such as K^+, Ag^+, Fe^{2+}/Fe^{3+}, and Al^{3+} were also used to fabricate PdCu nanochain networks,[39] Au nanorods,[40,41] Pt nanowires,[42] and CdSe nanocubes[43] by controlling the nanocrystal assembling and growth rate in the different crystallographic directions. However, to the best of our knowledge, hollow NFs have rarely been fabricated by cations because of the limited knowledge on the morphology-controlling ability of metal ions.

Herein, with the help of Ni^{2+} ion, we have successfully synthesized PtCu AONFs through a simple one-step hydrothermal process. In this evolution, there was a replacement reaction between solid Cu templates and Pt (IV) ion in aqueous and a selective deposition of resultant Pt and Cu atoms on the active sites.[44,45] Although Ni^{2+} did not incorporate in the NFs, it was essential in the formation of NFs structure due to the possible function in facilitating the

Received: January 29, 2019
Accepted: March 26, 2019
Published: March 26, 2019

DOI: 10.1021/acsaem.9b00205
ACS Appl. Energy Mater. 2019, 2, 2862−2869

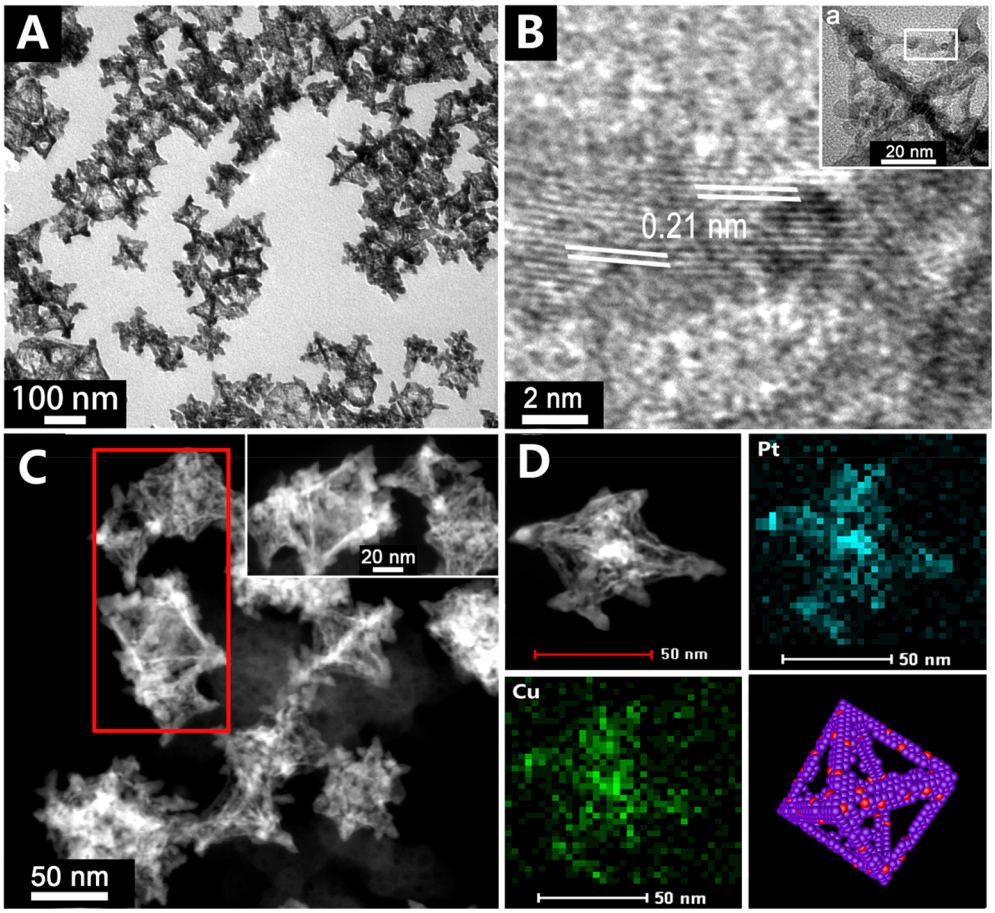

Figure 1. (A) TEM and (B) HRTEM images for the selected area in inset a of PtCu AONFs. (C) HAADF-STEM image of PtCu AONFs. (D) HAADF-STEM image and the corresponding EDS elemental mapping of a typical PtCu AONF, as well as a schematic illustration of a typical octahedral nanoframe structure, wherein the red particles represent Pt atoms and purple are Cu atoms.

diffusion of Cu atoms in replacement reaction.[46,47] The as-prepared PtCu AONFs not only maintained the advantages of the NFs architecture, but also had abundant highly anisotropic spiny nanothorns on the apexes of the octahedral which could offer highly dense of ridge, corner and step atoms.[34,35] So the as-prepared PtCu AONFs showed better activity and durability than commercial Pt/C for both ORR and MOR.[48,49]

2. EXPERIMENTAL SECTION

2.1. Chemicals. Glycine (99.5−100.5%), hexachloroplatinic acid hexahydrate ($H_2PtCl_6·6H_2O$, > 37.0%), nickel nitrate hexahydrate ($Ni(NO_3)_2·6H_2O$, > 98.0%), potassium iodide (KI, > 98.5%), ethanolamine (99.0−100.3%), potassium hydroxide (KOH, > 85.0%), methanol (>99.5%), ethanol (>99.7%) and perchloric acid ($HClO_4$, 70.0−72.0%) were purchased from Sinopharm Chemical Reagent Co., Ltd. Poly(vinylpyrrolidone) (PVP-40, M_w = 40 000) was purchased from Biosharp. Copper chloride dehydrate ($CuCl_2·2H_2O$, > 99.0%) was purchased from Shanghai Kechang Chemicals Company. 5.0 wt % of Nafion ethanol solution were purchased from Sigma-Aldrich. The ultrapure H_2O with a conductivity of 18.2 Ω/cm was obtained from the Direct-pure UP (Echo Pu International Ltd., USA). All of the chemicals in the experiment were not further purified.

2.2. Synthesis of PtCu AONFs with Abundant Spiny Nanothorns. In a typical synthesis, PVP-40 (0.10 g), KI (1.00 g, 6 mmol) and glycine (0.15 g, 2 mmol) were dissolved in 3.65 mL of H_2O with stirring, followed by the sequential adding of $H_2PtCl_6·6H_2O$ (20 mM, 1 mL), $CuCl_2·2H_2O$ (20 mM, 1 mL) and $Ni(NO_3)_2·6H_2O$ (20 mM, 0.335 mL). The color of solution changed from pale yellow to scarlet brown immediately. Then, 0.70 mL of ethanolamine was injected into the aforementioned solution and its color was gradually changed to light yellow-brown. After stirring it for 45 min, the resulting transparent yellow-green liquid was removed into a Teflon autoclave (25 mL) and treated at 160 °C for 16 h. After cooling to room temperature, the obtained black suspension was centrifuged with 12 000 rpm for 10 min to remove supernatant, followed by washing thrice with deionized H_2O and alcohol in turn to deduct surfactants and other contaminants. Finally, the cleaned products were redispersed in a 50% alcohol aqueous solution for subsequent characterization and electrochemical measurements.

2.3. Characterization. Transmission electron microscopy (TEM) images were taken from a JEM-2010 with 200 kV accelerating voltage, High-angle annular dark-field scanning transmission electron microscopy (HAADF-STEM) and high-resolution transmission electron microscopy (HRTEM) images were collected by using FEI Talos F200C at 200 kV. The XRD spectra were obtained by using Bruker D8 Advance X-ray diffractometer with Cu Kα radiation. The XPS result was measured by using a Thermo Scientific, ESCALAB 250Xi spectrophotometer with Al Kα X-ray radiation and standardized by using the C 1s peak (284.8 eV). The energy dispersive X-ray spectroscopy (EDS) elemental mapping was conducted on Tecnai G2 F30 and the data for inductively coupled plasma mass spectrometry (ICP-MS) was acquired via an Agilent-7900 ICP-MS system.

2.4. Electrochemical Measurements. To increase the specific surface area and conductivity of as-prepared electrocatalyst, about 2.0 mg of porous carbon materials were added to the as-prepared PtCu AONFs dispersion (about 0.2 mg), followed by ultrasonic assembling for 30 min to get carbon-supported PtCu AONFs catalyst.

DOI: 10.1021/acsaem.9b00205
ACS Appl. Energy Mater. 2019, 2, 2862−2869

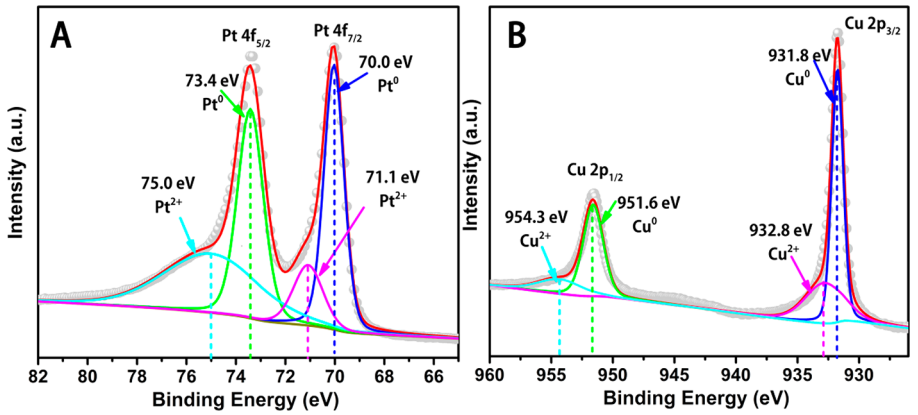

Figure 2. (A) Pt 4f and (B) Cu 2p XPS peaks of PtCu AONFs.

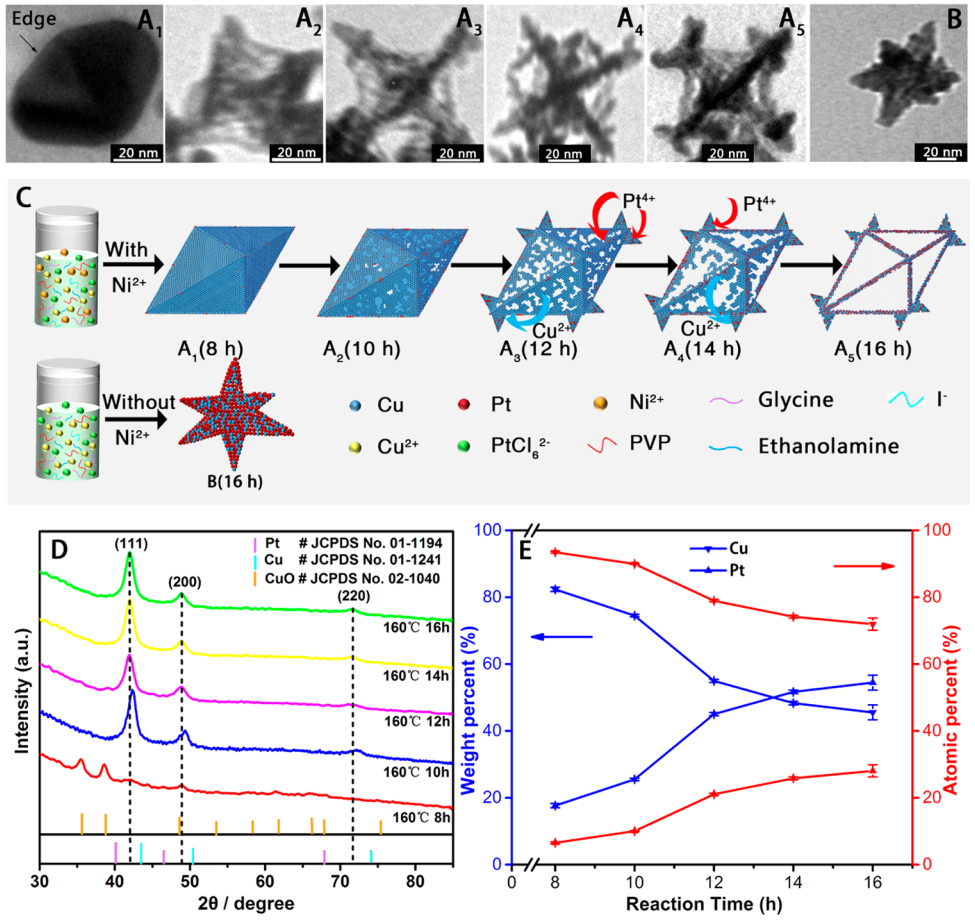

Figure 3. (A) TEM images of products with 335 μL Ni^{2+} at different reaction times: (A_1) 8, (A_2) 10, (A_3) 12, (A_4) 14, and (A_5) 16 h. (B) TEM image of the final products without Ni^{2+} for 16 h. (C) Schematic illustration of the corresponding (A, B) TEM images. (D, E) Plots represent the time-dependent XRD patterns and corresponding compositional evolution for the formation of PtCu AONFs with 335 μL Ni^{2+}.

The ORR electrochemical measurements for PtCu AONFs were carried out by combining Pine Modulated Speed Rotator (Pine, USA) with CHI 600B electrochemical workstation (Chenhua Instruments Corp, Shanghai). All measurements were carried out at 25 °C with a normal three electrode system, and its working, reference and counter electrodes were glass-carbon rotating disk electrode (RDE, 0.196 cm^2), Ag/AgCl and spiral Pt wire, respectively. Before test, the working electrode RDE was successively polished on the corresponding polishing plate with 1.0, 0.3, and 0.05 μm γ-aluminum oxide powder and then sonicated about 15 s in 50% HNO_3 solution. After blowing dry with N_2, the carbon-loaded PtCu AONFs dispersions were added dropwise on RDE surface and dried in air. The actual loading of Pt mass on the electrode was calculated by ICP-MS. Subsequently, 5.0 μL of diluted Nafion alcohol solution (0.5 wt %) were modified to the surface of PtCu AONFs-decorated RDE. After drying in air naturally, the ORR performance of carbon-loaded PtCu AONFs was measured in O_2-saturated 0.1 M $HClO_4$ aqueous with 10 mV/s scan speed and 1600 rpm rotation rate.

For MOR measurments, all electrochemical tests were recorded using the CHI 600D electrochemical workstation (Chenhua Instruments Corp, Shanghai). The working electrodes were conventional glassy carbon electrode (GCE, d = 3 mm). All glassy carbon electrodes were prepared in the same manner as the ORR mearsurements, followed by a modified 5.0 μL of carbon-loaded

DOI: 10.1021/acsaem.9b00205
ACS Appl. Energy Mater. 2019, 2, 2862−2869

PtCu AONFs on the GCE surface. Finally, 5.0 μL of diluted Nafion alcohol solution (0.5 wt %) were added dropwise on the surface. After drying, the MOR measurements were executed in 1 M of KOH aqueous consist of 1 M of CH_3OH at 50 mV/s scan speed.

The electrochemical measurements of commercial Pt/C were all similar to as-prepared PtCu AONFs. The Pt/C was prepared as follows: 5 mg of commercial Pt/C (JM, Pt 20 wt %) was added to 2 mL of alcohol aqueous solution (50 wt %) and sonicated around 1 h until the dispersion was homogeneous (Pt = 0.50 mg mL^{-1}).

3. RESULTS AND DISCUSSION

3.1. Material Characterization. The morphology of the obtained nanomaterials was first characterized by TEM. Figure 1A clearly showed the well-defined PtCu AONFs with abundant highly anisotropic spiny nanothorns on the apexes of the octahedral. For the most of PtCu AONFs (Figure 1A), the average length of the ridges was approximately 40 nm and the thickness of frames was about 8 nm, whereas the length of anisotropic spiny nanothorns was around 11 nm. The magnified HRTEM image in Figure 1B showed that the lattice fringe spacing was nearly 0.21 nm, which was attributed to the (111) plane of face-centered cubic (fcc) PtCu AONFs.[37,50] Moreover, their lattice spacing were slightly smaller than the (111) plane of fcc pure Pt crystal (0.226 nm), which indirectly indicated the formation of PtCu alloy.[51] As shown in HAADF-STEM image (Figure 1C, D), the homogeneous distribution of Pt and Cu elements on the whole nanostructure further indicated the alloy nature of PtCu AONFs.[44,51] Besides, the elemental composition of acquired products was also analyzed via ICP-MS technology. The as-prepared PtCu AONFs had an atomic ratio of platinum to copper of approximately 28.0/72.0, i.e., $Pt_{28}Cu_{72}$ AONFs and no Ni element was existed. The EDS spectrum showed that the PtCu AONF was a Cu-rich structure (Figure S1), in accordance with the previously mentioned ICP-MS data.

The XPS spectra were used to characterize the surface composition and surface chemical states of PtCu AONFs (Figure 2 and Figure S2). As shown in Figure 2A, the binding energies of Pt $4f_{7/2}$ and Pt $4f_{5/2}$ for PtCu AONFs were located at 70.0 and 73.4 eV, respectively, which were evidently lower than that of pure Pt (71.1 eV, 74.6 eV).[52] The decrease in Pt 4f binding energy confirm the changes in surface electronic structure of Pt, which could be attributed to the surface electronic interaction between Pt and Cu.[50−52] After peak fitting, it was confirmed that there were Pt^0 and Pt^{2+} two valence states and the majority of Pt atoms were metal state on PtCu AONFs surface.[51,52] Meanwhile, the typical Cu 2p peaks in Figure 2B were also fitted into Cu^0 $2p_{3/2}$ (931.8 eV), Cu^{2+} $2p_{3/2}$ (932.8 eV), Cu^0 $2p_{1/2}$ (951.6 eV), and $Cu^{2+}2p_{1/2}$ (954.3 eV) respectively. And according to the peaks intensity, it suggested that Cu atoms were also mainly Cu^0 state.[50,51] The XRD pattern (Figure S3) of PtCu AONFs demonstrated that the 2θ values of the main diffraction peaks were located at the (111), (200), and (220) planes, and the diffraction peak accounting for the dominant advantage was derived from the (111) plane corresponding to the classic fcc structure, which is consistent with the HRTEM results. At the same time, every diffraction peak were existed between pure Pt (JCPDS: 01−1194) and pure Cu (JCPDS: 01−1241), indicating the formation of PtCu alloy nanocrystals.[22,37,50,51,53,54]

The time-evolution TEM images were used to observe the forming process of PtCu AONFs with abundant highly anisotropic spiny nanothorns (Figure 3A, Table S2). In the presence of Ni^{2+}, solid Cu octahedral templates with an average edge length about 40 nm were first formed in the initial stage because of the higher reduction rate of Cu^{2+} than $PtCl_6^{2-}$, which was tuned by glycine (Figure $3A_1$ and $3CA_1$).[35,44,45] The formation of Cu intermediate was characterized by XRD analysis. Because of the unstable Cu intermediate was easily oxidized under air condition, only the characteristic diffraction peak of CuO (JCPDS: 02−1040) was detected (Figure 3D).[44,55,56] The ICP-MS data (Figure 3E) also confirmed that Cu was indeed the prominent component of the solid octahedral templates (atomic ratio of Cu 93.5% and Pt 6.5%). As the reaction went on, hollow structures were gradually formed because of the replacement reaction between Cu templates and $PtCl_6^{2-}$ in the aqueous.[11,12,35] Additionally, the coreduction of $PtCl_6^{2-}$ (H_2PtCl_6) and Cu^{2+} (dissolved from solid Cu octahedron) also occurred during the replacement reaction and the resulting Pt and Cu atoms selectively deposited on the apexes whose atoms were more active than other places, leading to the growth of spiny nanothorns (Figure $3A_2$−A_4 and $3CA_2$−CA_4).[35,53] The emerging PtCu alloy characteristic diffraction peaks and the disappearance of CuO characteristic diffraction peak in XRD results also proved the formation of Pt composition in those intermediates during the replacement reaction (Figure 3D). The same trend can also be found in the ICP-MS results (Figure 3E). After reaction for 16 h, the final PtCu AONFs were formed, which possessed dense spiny nanothorns from the apexes (Figure $3A_5$ and CA_5).

However, in the absence of Ni^{2+}, only concave octahedral solid nanocrystals existed in the final products in a similar condition of aforementioned reaction (Figure 3B and Figure S4a). To verify the Ni^{2+} effect of forming hollow structure, we added different amounts of Ni^{2+} in this hydrothermal reaction (Table S3). As shown in Figure S4, the hollow structure of the final products became more obvious with the rise of Ni^{2+} concentration. Therefore, we speculated that Ni^{2+} may facilitate the diffusion of Cu atoms during the replacement reaction, leading to the formation of hollow structure.[46,57,58] The adsorption of Ni ion on the surface of Cu atom alters the surface energy of Cu nanoparticles, accelerating the displacement reduction rate of the adsorbed Pt^{4+} precursor and the diffusion of Cu atoms.[59,60]

To verify this hypothesis, we analyzed the composition of PtCu solid concave octahedrons synthesized without Ni^{2+} ion by ICP-MS. As shown in Table S4, the Cu/Pt atomic ratio was approximately 79:21, which was higher than that of PtCu hollow NFs synthesized with Ni^{2+} (72:28). Therefore, the lower Cu amount in PtCu hollow NFs indicated a higher diffusion release of Cu atoms in the presence of Ni^{2+}. The effect of Cu atoms diffusion rate on forming hollow structure was also verified by changing the reaction temperature (Table S5). Generally, a higher temperature would cause a quicker diffusion rate in a reaction.[36,47,58] As shown in Figure S5, when the temperature was increased to 180 °C, the hollow structure emerged even in the absence of Ni^{2+}, and when the temperature further rose to 200 °C, the hollow structure became more obvious but the dispersibility and specific surface area decreased.

3.2. Evaluations of Electrochemical Performance. The electrochemically active surface areas (ECSA) of spiny PtCu AONFs was calculated by the hydrogen adsorption/desorption region of cyclic voltammograms (CVs) in Figure S6 tested in N_2-saturated 0.1 M $HClO_4$ aqueous solution with a sweep speed of 50 mV/s.[14,54] The mass of Pt loaded on the rotating

DOI: 10.1021/acsaem.9b00205
ACS Appl. Energy Mater. 2019, 2, 2862−2869

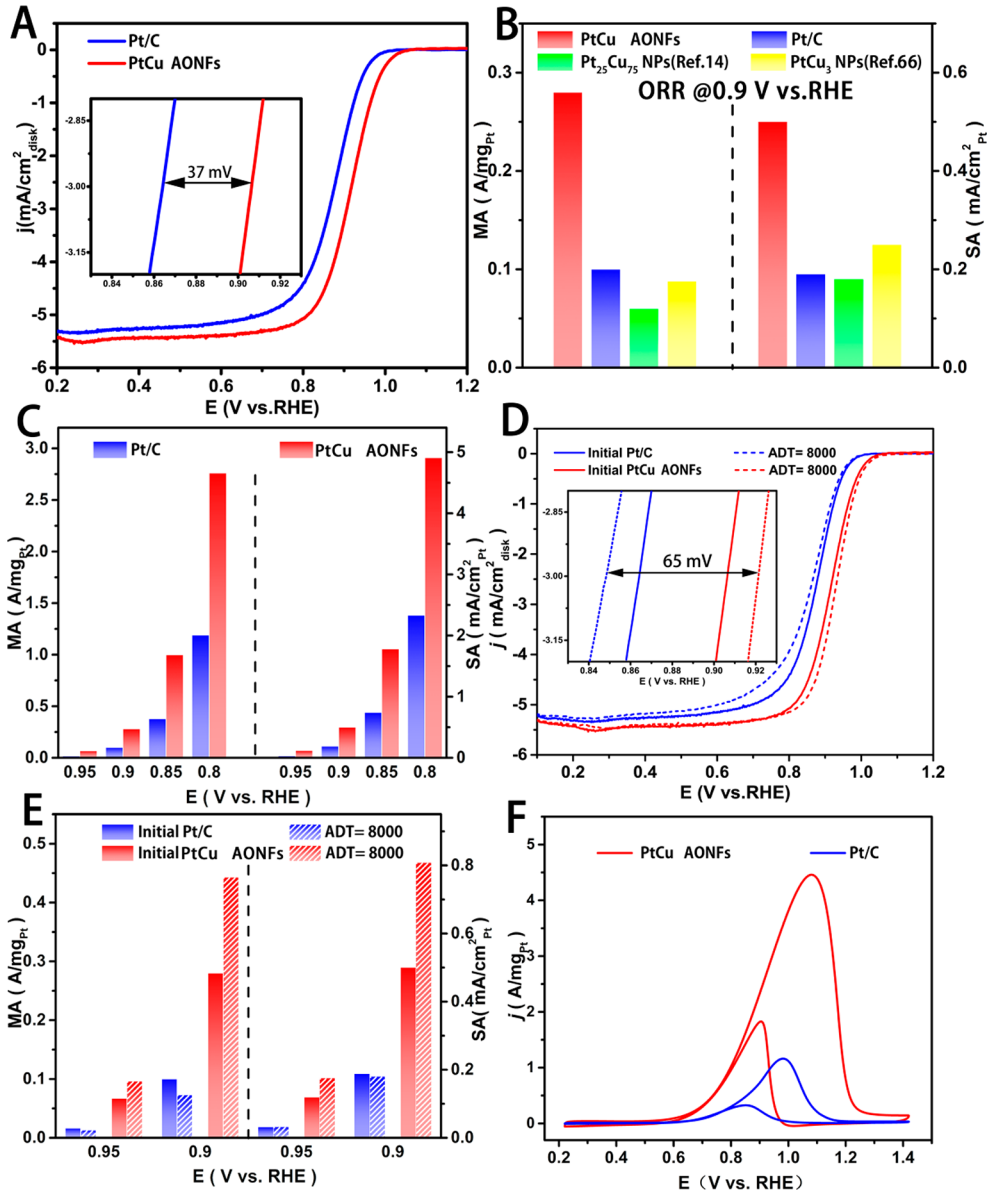

Figure 4. (A) ORR polarization curves of PtCu AONFs and Pt/C. (B) Comparison of MA and SA for PtCu AONFs, $Pt_{25}Cu_{75}$ NPs,[14] $PtCu_3$ NPs[66] and Pt/C at 0.9 V vs RHE. (C) MA and SA for PtCu AONFs and Pt/C at different potential vs RHE. (D) ORR polarizations of PtCu AONFs and Pt/C before and after ADT. (E) MA and SA before and after the ADT at 0.95 and 0.9 V vs RHE, respectively. (F) CV curves of PtCu AONFs and Pt/C in 1 M KOH and 1 M methanol. In A and D, j (mA/cm^2) were normalized in reference to the electrode geometric area (0.196 cm^2).

disk electrode normalized by the geometrical area of the glassy carbon were 28.7 and 27.7 μg/cm^2 for PtCu AONFs and Pt/C. After correcting the double-layer and assuming a value of 210 μC cm^{-2} for the adsorption of a hydrogen monolayer, the ECSA of spiny PtCu AONFs and commercial Pt/C were 56.2 and 55.3 m^2/g$_{Pt}$, respectively (eq S1, Table S6).

The ORR measurements of spiny PtCu AONFs and commercial Pt/C was tested in an O_2-saturated 0.1 M $HClO_4$ aqueous solution at a sweep rate of 10 mV/s with a rotation rate of 1600 rpm. The spiny PtCu AONFs showed the higher diffusion-limiting current density (~5.50 mA/cm^2) and more positive half-wave potential (~0.914 V vs RHE,) than Pt/C (Figure 4A, Table S6). There were 37.0 mV differences for half-wave potential between PtCu AONFs and Pt/C, which exhibited that PtCu AONFs had an ideal ORR overpotential and implied superior catalytic activity for ORR.[52,54,61,62] According to MA and SA Tafel plots as exhibited in Figure S7, PtCu AONFs possessed higher current density under the same potential compared to Pt/C. Their kinetic current was calculated based on the Koutecky−Levich equation (eq S2).[52,54,63−65] Figure 4B is a columnar comparison of MA and SA for ORR of PtCu AONFs and Pt/C at 0.9 V vs RHE and included two reported PtCu NPs: $Pt_{25}Cu_{75}$ NPs[14] and $PtCu_3$ NPs.[66] The MA and SA for PtCu AONFs were 0.28 A/mg$_{Pt}$ and 0.50 mA/cm^2, which are approximately 2.8 and 2.6 times that of to Pt/C (0.10 A/mg$_{Pt}$, 0.19 mA/cm^2), respectively. Meanwhile, the superiority of hollow NFs to solid NPs is reflected with the two reported PtCu solid NPs ($Pt_{25}Cu_{75}$ NPs,[14] 0.06 A/mg$_{Pt}$, 0.18 mA/cm^2, $PtCu_3$ NPs,[66] 0.088 A/mg$_{Pt}$, 0.25 mA/cm^2). The MA and SA of PtCu AONFs as shown in Figure 4C were all higher than Pt/C at different potential. Furthermore, we also collected and listed a large number of ORR mass activities of other reported Pt-based nanomaterials in Table S7. The enhanced ORR

DOI: 10.1021/acsaem.9b00205
ACS Appl. Energy Mater. 2019, 2, 2862−2869

performance can be attributed to following issues: first, the hollow nanoframe structure increased Pt-based catalyst specific surface area.[35−37] Second, the anisotropic spiny nanothorns provided more active site, such as edge, corner and step atoms.[34,35,44,50,51] Third, the PtCu alloy changed the surface electronic structure of pure Pt catalyst, which could greatly push forward the electrocatalytic performance toward ORR owing to the decline of adsorption energy between Pt and O.[44,67,68]

In addition, the durability of PtCu AONFs was evaluated in O_2-saturated 0.1 M $HClO_4$ aqueous solution at a scan rate of 50 mV/s and a rotation rate of 1600 rpm. After 8000 cycles of the accelerated durability test (ADT) were measured at the potential between 0.60 and 1.0 V vs RHE, PtCu AONFs held the lesser decline for ECSA/g_{Pt} (54.8 m^2/g_{Pt}, Figures S8 and S9), which only reduced by 1.19 m^2/g_{Pt} (2.10%) in comparison to original (56.2 m^2/g_{Pt}). The ECSA/g_{Pt} for Pt/C after 8000 cycles was 43.9 m^2/g_{Pt}, which decreased by 11.4 m^2/g_{Pt} (20.5%) compared with the initial value (55.3 m^2/g_{Pt}). Figure 4D was ORR polarization for PtCu AONFs before and after 8000 cycles. It showed better half-wave potential (0.929 V) for PtCu AONFs, which were 65.0 mV higher than Pt/C (0.864 V) after ADT (Figure 4D, Figure S9). The PtCu AONFs had better durability than Pt/C according to Figure 4E and Figure S10 before and after ADT at 0.80, 0.85, 0.90, and 0.95 V vs RHE, and the Tafel plots also proved this conclusion (Figure S11). Their MA (0.096 A/mg_{Pt}) and SA (0.18 mA/cm^2) after ADT of PtCu AONFs were 7.4 and 5.6 times corresponding to that of Pt/C (0.013 A/mg_{Pt}, 0.032 mA/cm^2) at 0.95 V vs RHE. Meanwhile, the MA (0.44 A/mg $_{Pt}$) and SA (0.81 mA/cm^2) at 0.90 V vs RHE were 6.0 and 4.5 times than Pt/C (0.073 A/mg_{Pt}, 0.18 mA/cm^2). Surfactant and specific surface area may be the reason for the increase of ORR activity. In a typical characterization, the PtCu AONFs were directly added on the electrode to make ADT test without the mix of carbon support. The XPS characterization showed that the chemical state of PtCu structure did not change (Figure S13), but the atom ratio of C on the surface of catalyst decreased from 72.8% to 42.2% after the ADT test. Due to the absence of carbon support, the content of C was derived from surfactant (PVP). Additionally, from the TEM and HRTEM characterization (Figure S12), the microstructures of PtCu AONF did not change after the ADT test, ruling out the possible effect of specific surface area. Therefore, the increase of ORR activity could be attributed to the clearance of surfactant on the surface of catalysts during the ADT test, increasing the exposure of active sites.[69,70]

For the MOR, the loaded quantities were 39.5 and 35.4 $\mu g/cm^2$ for PtCu AONFs and Pt/C. First, the catalysts modified on GCE were first activated in 0.1 M $HClO_4$ aqueous. The obtained CV curve (Figure S14) was used to calculate the ECSA (PtCu AONFs: 57.3 $m^2/g_{Pt;}$ Pt/C: 54.3m^2/g_{Pt}). Then, the CV curves (Figure 4F, Figure S15) normalized with respect to the loaded-Pt mass or ECSA were tested in 1 M KOH and 1 M methanol and PtCu AONFs showed better MOR catalytic activity than Pt/C. The MA and SA of PtCu AONFs were 4.46 A/mg_{Pt} and 7.78 mA/cm^2, which were nearly 3.80 and 3.60 times than Pt/C (1.16 A/mg_{Pt}, 2.14 mA/cm^2) as show in Figure S16. Meanwhile, the MOR mass activity of the PtCu AONFs and various of reported Pt-based nanomaterials are listed in Table S8. PtCu AONFs also showed good electrocatalytic activity toward MOR, which may closely related to the aforementioned synergy mentioned.[18,22] The Amperometric i-t curve (Figure S17) was used to evaluate the catalytic endurance of the catalysts. The current density of Pt/C sharply decreased from the beginning, whereas the PtCu AONFs maintained higher current density compared to Pt/C during 5000 s. The above results reveal that the PtCu AONFs have the better catalytic endurance.

4. CONCLUSIONS

In this study, a nickel-ion-oriented one-step hydrothermal method was adopted to prepare the well-defined PtCu bimetallic alloy octahedral nanoframes with abundant spiny nanothorns on the apexes. Ni^{2+} metal ion played a pivotal role in forming hollow structure due to the acceleration of Cu atom diffusion during the replacement reaction between Cu intermediate and Pt precursors. And the formation of spiny nanothorns was attributed to the selective deposition of Pt and Cu atoms in active sites. The as-prepared spiny PtCu AONFs exhibit higher electrochemical catalytic activity and durability for ORR and MOR than Pt/C and other reported Pt-based nanostructures. This method offered a new potential approach to fabricate other hollow structures, expanding the utilization of metal ions in nanoarchitecture.

■ ASSOCIATED CONTENT

Supporting Information

The Supporting Information is available free of charge on the ACS Publications website at DOI: 10.1021/acsaem.9b00205.

Additional characterization data, including EDS, TEM, HRTEM, XPS, XRD, CV, and Tafel plots; data tables; and electrochemical calculations (PDF)

■ AUTHOR INFORMATION

Corresponding Author

*E-mail: hyhan@mail.hzau.edu.cn.

ORCID

Heyou Han: 0000-0001-9406-0722

Author Contributions

†G.Z. and J.L. contributed equally to this work.

Notes

The authors declare no competing financial interest.

■ ACKNOWLEDGMENTS

The authors acknowledge financial support from Science and Technology Major Project of Guangxi (Gui Ke AA18118046), National Key R&D Program of China (2016YFD0500706), National Natural Science Foundation of China (21778020), and Sci-tech Innovation Foundation of Huazhong Agriculture University (2662017PY042, 2662018PY024).

■ REFERENCES

(1) Grey, C. P.; Tarascon, J. M. Sustainability and in Situ Monitoring in Battery Development. *Nat. Mater.* **2017**, *16*, 45−56.

(2) Stamenkovic, V. R.; Strmcnik, D.; Lopes, P. P.; Markovic, N. M. Energy and Fuels from Electrochemical Interfaces. *Nat. Mater.* **2017**, *16*, 57−69.

(3) Hu, S.; Munoz, F.; Noborikawa, J.; Haan, J.; Scudiero, L.; Ha, S. Carbon Supported Pd-Based Bimetallic and Trimetallic Catalyst for Formic Acid Electrochemical Oxidation. *Appl. Catal., B* **2016**, *180*, 758−765.

(4) Wee, J.-H. Applications of Proton Exchange Membrane Fuel Cell Systems. *Renewable Sustainable Energy Rev.* **2007**, *11*, 1720−1738.

DOI: 10.1021/acsaem.9b00205
ACS Appl. Energy Mater. 2019, 2, 2862−2869

(5) Wang, Y.; Chen, K. S.; Mishler, J.; Cho, S. C.; Adroher, X. C. A Review of Polymer Electrolyte Membrane Fuel Cells: Technology, Applications, and Needs on Fundamental Research. *Appl. Energy* **2011**, *88*, 981−1007.
(6) Scofield, M. E.; Liu, H.; Wong, S. S. A Concise Guide to Sustainable PEMFCs: Recent Advances in Improving both Oxygen Reduction Catalysts and Proton Exchange Membranes. *Chem. Soc. Rev.* **2015**, *44*, 5836−5860.
(7) Becknell, N.; Kang, Y.; Chen, C.; Resasco, J.; Kornienko, N.; Guo, J.; Markovic, N. M.; Somorjai, G. A.; Stamenkovic, V. R.; Yang, P. Atomic Structure of Pt_3Ni Nanoframe Electrocatalysts by in Situ X-Ray Absorption Spectroscopy. *J. Am. Chem. Soc.* **2015**, *137*, 15817−15824.
(8) Saha, M. S.; Neburchilov, V.; Ghosh, D.; Zhang, J. Nanomaterials-Supported Pt Catalysts for Proton Exchange Membrane Fuel Cells. *WIREs Energy Environ.* **2013**, *2*, 31−51.
(9) Liu, J. W.; Zheng, Y.; Hong, Z. L.; Cai, K.; Zhao, F.; Han, H. Y. Microbial synthesis of highly dispersed PdAu alloy for enhanced electrocatalysis. *Sci. Adv.* **2016**, *2*, No. e1600858.
(10) Xia, Y.; Xiong, Y.; Lim, B.; Skrabalak, S. E. Shape-Controlled Synthesis of Metal Nanocrystals: Simple Chemistry Meets Complex Physics? *Angew. Chem., Int. Ed.* **2009**, *48*, 60−103.
(11) Qu, J.; Ye, F.; Chen, D.; Feng, Y.; Yao, Q.; Liu, H.; Xie, J.; Yang, J. Platinum-Based Heterogeneous Nanomaterials Via Wet-Chemistry Approaches Toward Electrocatalytic Applications. *Adv. Colloid Interface Sci.* **2016**, *230*, 29−53.
(12) Gilroy, K. D.; Ruditskiy, A.; Peng, H. C.; Qin, D.; Xia, Y. Bimetallic Nanocrystals: Syntheses, Properties, and Applications. *Chem. Rev.* **2016**, *116*, 10414−10472.
(13) Wang, Y. J.; Zhao, N.; Fang, B.; Li, H.; Bi, X. T.; Wang, H. Carbon-Supported Pt-Based Alloy Electrocatalysts for the Oxygen Reduction Reaction in Polymer Electrolyte Membrane Fuel Cells: Particle Size, Shape, and Composition Manipulation and Their Impact to Activity. *Chem. Rev.* **2015**, *115*, 3433−3467.
(14) Fu, S.; Zhu, C.; Shi, Q.; Du, D.; Lin, Y. Enhanced Electrocatalytic Activities of Three Dimensional PtCu@Pt Bimetallic Alloy Nanofoams for Oxygen Reduction Reaction. *Catal. Sci. Technol.* **2016**, *6*, 5052−5059.
(15) Lim, B.; Jiang, M.; Camargo, P. H.C.; Cho, E.; Tao, J.; Lu, X.; Zhu, Y.; Xia, Y. Pd-Pt Bimetallic Nanodendrites with High Activity for Oxygen Reduction. *Science* **2009**, *324*, 1302−1305.
(16) Hu, C.; Cheng, H.; Zhao, Y.; Hu, Y.; Liu, Y.; Dai, L.; Qu, L. Newly-Designed Complex Ternary Pt/PdCu Nanoboxes Anchored on Three-Dimensional Graphene Framework for Highly Efficient Ethanol Oxidation. *Adv. Mater.* **2012**, *24*, 5493−5498.
(17) Antolini, E. Formation of Carbon-Supported PtM Alloys for Low Temperature Fuel Cells. *Mater. Chem. Phys.* **2003**, *78*, 563−573.
(18) Luo, S.; Shen, K. P. Concave Platinum-Copper Octopod Nanoframes Bounded with Multiple High-Index Facets for Efficient Electrooxidation Catalysis. *ACS Nano* **2017**, *11*, 11946.
(19) Becknell, N.; Zheng, C.; Chen, C.; Yu, Y.; Yang, P. Synthesis of $PtCo_3$ Polyhedral Nanoparticles and Evolution to Pt_3Co Nanoframes. *Surf. Sci.* **2016**, *648*, 328−332.
(20) Zhang, N.; Bu, L.; Guo, S.; Guo, J.; Huang, X. Screw Thread-Like Platinum-Copper Nanowires Bounded with High-Index Facets for Efficient Electrocatalysis. *Nano Lett.* **2016**, *16*, 5037−5043.
(21) Jia, Y.; Jiang, Y.; Zhang, J.; Zhang, L.; Chen, Q.; Xie, Z.; Zheng, L. Unique Excavated Rhombic Dodecahedral $PtCu_3$ Alloy Nanocrystals Constructed with Ultrathin Nanosheets of High-Energy {110} Facets. *J. Am. Chem. Soc.* **2014**, *136*, 3748−3751.
(22) Xia, B. Y.; Wu, H. B.; Wang, X.; Lou, X. W. One-Pot Synthesis of Cubic $PtCu_3$ Nanocages with Enhanced Electrocatalytic Activity for the Methanol Oxidation Reaction. *J. Am. Chem. Soc.* **2012**, *134*, 13934−13937.
(23) Fu, S.; Zhu, C.; Shi, Q.; Xia, H.; Du, D.; Lin, Y. Highly branched PtCu bimetallic alloy nanodendrites with superior electrocatalytic activities for oxygen reduction reactions. *Nanoscale* **2016**, *8*, 5076−5081.
(24) He, D.; Zhang, L.; He, D.; Zhou, G.; Lin, Y.; Deng, Z.; Hong, X.; Wu, Y.; Chen, C.; Li, Y. Amorphous Nickel Boride Membrane on a Platinum-Nickel Alloy Surface for Enhanced Oxygen Reduction Reaction. *Nat. Commun.* **2016**, *7*, 12362.
(25) Duan, H.; Yan, N.; Yu, R.; Chang, C. R.; Zhou, G.; Hu, H. S.; Rong, H.; Niu, Z.; Mao, J.; Asakura, H.; Tanaka, T.; Dyson, P. J.; Li, J.; Li, Y. Ultrathin Rhodium Nanosheets. *Nat. Commun.* **2014**, *5*, 3093.
(26) Zhao, M.; Wang, Y.; Ma, Q.; Huang, Y.; Zhang, X.; Ping, J.; Zhang, Z.; Lu, Q.; Yu, Y.; Xu, H.; Zhao, Y.; Zhang, H. Ultrathin 2D Metal-Organic Framework Nanosheets. *Adv. Mater.* **2015**, *27*, 7372−7378.
(27) Nikoobakht, B.; El-Sayed, M. A. Evidence for Bilayer Assembly of Cationic Surfactants on the Surface of Gold Nanorods. *Langmuir* **2001**, *17*, 6368−6374.
(28) Cai, K.; Lv, Z.; Chen, K.; Huang, L.; Wang, J.; Shao, F.; Wang, Y.; Han, H. Aqueous Synthesis of Porous Platinum Nanotubes at Room Temperature and Their Intrinsic Peroxidase-Like Activity. *Chem. Commun.* **2013**, *49*, 6024−6026.
(29) Zuo, Y.; Cai, K.; Wu, L.; Li, T.; Lv, Z.; Liu, J.; Shao, K.; Han, H. Spiny-Porous Platinum Nanotubes with Enhanced Electrocatalytic Activity for Methanol Oxidation. *J. Mater. Chem. A* **2015**, *3*, 1388−1391.
(30) Wang, L.; Yamauchi, Y. Metallic Nanocages: Synthesis of Bimetallic Pt-Pd Hollow Nanoparticles with Dendritic Shells by Selective Chemical Etching. *J. Am. Chem. Soc.* **2013**, *135*, 16762−16765.
(31) Wang, X.; Choi, S.-I.; Roling, L. T.; Luo, M.; Ma, C.; Zhang, L.; Chi, M.; Liu, J.; Xie, Z.; Herron, J. A.; Mavrikakis, M.; Xia, Y. Palladium-Platinum Core-Shell Icosahedra with Substantially Enhanced Activity and Durability Towards Oxygen Reduction. *Nat. Commun.* **2015**, *6*, 7594−7602.
(32) Wang, X.; Vara, M.; Luo, M.; Huang, H.; Ruditskiy, A.; Park, J.; Bao, S.; Liu, J.; Howe, J.; Chi, M.; Xie, Z.; Xia, Y. Pd@Pt Core-Shell Concave Decahedra: A Class of Catalysts for the Oxygen Reduction Reaction with Enhanced Activity and Durability. *J. Am. Chem. Soc.* **2015**, *137*, 15036−15042.
(33) Hong, X.; Wang, D.; Cai, S.; Rong, H.; Li, Y. Single-Crystalline octahedral Au-Ag Nanoframes. *J. Am. Chem. Soc.* **2012**, *134*, 18165−18168.
(34) Luo, S.; Tang, M.; Shen, P. K.; Ye, S. Atomic-Scale Preparation of Octopod Nanoframes with High-Index Facets as Highly Active and Stable Catalysts. *Adv. Mater.* **2017**, *29*, 1601687.
(35) Fang, Z.; Wang, Y.; Liu, C.; Chen, S.; Sang, W.; Wang, C.; Zeng, J. Rational Design of Metal Nanoframes for Catalysis and Plasmonics. *Small* **2015**, *11*, 2593−2605.
(36) Chen, C.; Kang, Y.; Huo, Z.; Zhu, Z.; Huang, W.; Xin, H. L.; Snyder, J. D.; Li, D.; Herron, J. A.; Mavrikakis, M.; Chi, M.; More, K. L.; Li, Y.; Markovic, N. M.; Somorjai, G. A.; Yang, P.; Stamenkovic, V. R. Highly Crystalline Multimetallic Nanoframes with Three-Dimensional Electrocatalytic Surfaces. *Science* **2014**, *343*, 1339−1343.
(37) Ding, J.; Zhu, X.; Bu, L.; Yao, J.; Guo, J.; Guo, S.; Huang, X. Highly Open Rhombic Dodecahedral PtCu Nanoframes. *Chem. Commun.* **2015**, *51*, 9722−9725.
(38) Lyu, L.-M.; Kao, Y.-C.; Cullen, D. A.; Sneed, B. T.; Chuang, Y.-C.; Kuo, C.-H. Spiny Rhombic Dodecahedral CuPt Nanoframes with Enhanced Catalytic Performance Synthesized from Cu Nanocube Templates. *Chem. Mater.* **2017**, *29*, 5681−5692.
(39) Liu, J.; Huang, Z.; Cai, K.; Zhang, H.; Lu, Z.; Li, T.; Zuo, Y.; Han, H. Clean Synthesis of an Economical 3D Nanochain Network of PdCu Alloy with Enhanced Electrocatalytic Performance towards Ethanol Oxidation. *Chem. - Eur. J.* **2015**, *21*, 17779−17785.
(40) Jana, N. R.; Gearheart, L.; Murphy, C. J. Wet Chemical Synthesis of High Aspect Ratio Cylindrical Gold Nanorods. *J. Phys. Chem. B* **2001**, *105*, 4065−4067.
(41) Pérez-Juste, J.; Pastoriza-Santos, I.; Liz-Marzán, L. M.; Mulvaney, P. Gold Nanorods: Synthesis, Characterization and Applications. *Coord. Chem. Rev.* **2005**, *249*, 1870−1901.

DOI: 10.1021/acsaem.9b00205
ACS Appl. Energy Mater. 2019, 2, 2862−2869

(42) Chen, J.; Herricks, T.; Xia, Y. Polyol Synthesis of Platinum Nanostructures: Control of Morphology through the Manipulation of Reduction Kinetics. *Angew. Chem., Int. Ed.* **2005**, *44*, 2589−2592.
(43) Li, W.; Zamani, R.; Ibanez, M.; Cadavid, D.; Shavel, A.; Morante, J. R.; Arbiol, J.; Cabot, A. Metal Ions to Control the Morphology of Semiconductor Nanoparticles: Copper Selenide Nanocubes. *J. Am. Chem. Soc.* **2013**, *135*, 4664−4667.
(44) Zhang, Z.; Luo, Z.; Chen, B.; Wei, C.; Zhao, J.; Chen, J.; Zhang, X.; Lai, Z.; Fan, Z.; Tan, C.; Zhao, M.; Lu, Q.; Li, B.; Zong, Y.; Yan, C.; Wang, G.; Xu, Z. J.; Zhang, H. One-Pot Synthesis of Highly Anisotropic Five-Fold-Twinned PtCu Nanoframes Used as a Bifunctional Electrocatalyst for Oxygen Reduction and Methanol Oxidation. *Adv. Mater.* **2016**, *28*, 8712−8717.
(45) Nosheen, F.; Zhang, Z. C.; Zhuang, J.; Wang, X. One-Pot Fabrication of Single-Crystalline Octahedral Pt-Cu Nanoframes and Their Enhanced Electrocatalytic Activity. *Nanoscale* **2013**, *5*, 3660−3663.
(46) Moreau, L. M.; Schurman, C. A.; Kewalramani, S.; Shahjamali, M. M.; Mirkin, C. A.; Bedzyk, M. J. How Ag Nanospheres Are Transformed into AgAu Nanocages. *J. Am. Chem. Soc.* **2017**, *139*, 12291−12298.
(47) Osowiecki, W. T.; Ye, X.; Satish, P.; Bustillo, K. C.; Clark, E. L.; Alivisatos, A. P. Tailoring Morphology of Cu-Ag Nanocrescents and Core-Shell Nanocrystals Guided by a Thermodynamic Model. *J. Am. Chem. Soc.* **2018**, *140*, 8569−8577.
(48) Wu, Y.; Wang, D.; Zhou, G.; Yu, R.; Chen, C.; Li, Y. Sophisticated construction of Au islands on Pt-Ni: an ideal trimetallic nanoframe catalyst. *J. Am. Chem. Soc.* **2014**, *136*, 11594−11597.
(49) Kwon, T.; Jun, M.; Kim, H. Y.; Oh, A.; Park, J.; Baik, H.; Joo, S. H.; Lee, K. Vertex-Reinforced PtCuCo Ternary Nanoframes as Efficient and Stable Electrocatalysts for the Oxygen Reduction Reaction and the Methanol Oxidation Reaction. *Adv. Funct. Mater.* **2018**, *28*, 1706440.
(50) Zhang, J.; Ma, J.; Wan, Y.; Jiang, J.; Zhao, X. S. Dendritic Pt-Cu Bimetallic Nanocrystals with a High Electrocatalytic Activity Toward Methanol Oxidation. *Mater. Chem. Phys.* **2012**, *132*, 244−247.
(51) Gong, M.; Fu, G.; Chen, Y.; Tang, Y.; Lu, T. Autocatalysis and selective oxidative etching induced synthesis of platinum-copper bimetallic alloy nanodendrites electrocatalysts. *ACS Appl. Mater. Interfaces* **2014**, *6*, 7301−7308.
(52) Wang, H.; Wang, R.; Li, H.; Wang, Q.; Kang, J.; Lei, Z. Facile Synthesis of Carbon-Supported Pseudo-Core@Shell PdCu@Pt Nanoparticles for Direct Methanol Fuel Cells. *Int. J. Hydrogen Energy* **2011**, *36*, 839−848.
(53) Taylor, E.; Chen, S.; Tao, J.; Wu, L.; Zhu, Y.; Chen, J. Synthesis of Pt-Cu Nanodendrites Through Controlled Reduction Kinetics for Enhanced Methanol Electro-Oxidation. *ChemSusChem* **2013**, *6*, 1863−1867.
(54) Su, L.; Shrestha, S.; Zhang, Z.; Mustain, W.; Lei, Y. Platinum-Copper Nanotube Electrocatalyst with Enhanced Activity and Durability for Oxygen Reduction Reactions. *J. Mater. Chem. A* **2013**, *1*, 12293.
(55) Hosseini, M.; Fatmehsari, D. H.; Marashi, S. P. H. Synthesis of Different Copper Nanostructures by The Use of Polyol Technique. *Appl. Phys. A: Mater. Sci. Process.* **2015**, *120*, 1579−1586.
(56) Preston, A. S.; Hughes, R. A.; Demille, T. B.; Neretina, S. Copper Template Design for the Synthesis of Bimetallic Copper-Rhodium Nanoshells through Galvanic Replacement. *Part. Part. Syst. Charact.* **2018**, *35*, 1700420.
(57) Xu, C.; Liu, Y.; Wang, J.; Geng, H.; Qiu, H. Nanoporous PdCu Alloy for Formic Acid Electro-Oxidation. *J. Power Sources* **2012**, *199*, 124−131.
(58) Han, L.; Wang, P.; Liu, H.; Tan, Q.; Yang, J. Balancing the Galvanic Replacement and Reduction Kinetics for The General Formation of Bimetallic CuM (M = Ru, Rh, Pd, Os, Ir, and Pt) Hollow Nanostructures. *J. Mater. Chem. A* **2016**, *4*, 18354−18365.
(59) Moghimi, N.; Abdellah, M.; Thomas, J. P.; Mohapatra, M.; Leung, K. T. Bimetallic FeNi concave nanocubes and nanocages. *J. Am. Chem. Soc.* **2013**, *135*, 10958−10961.
(60) Vaes, J.; Fransaer, J.; Celis, J. P. The Role of Metal Hydroxides in NiFe Deposition. *J. Electrochem. Soc.* **2000**, *147*, 3718−3724.
(61) Li, M.; Zhao, Z.; Cheng, T.; Fortunelli, A.; Chen, C.-Y.; Yu, R.; Zhang, Q.; Gu, L.; Merinov, B.; Lin, Z.; Zhu, E.; Yu, T.; Jia, Q.; Guo, J.; Zhang, L.; Goddard, W. A.; Huang, Y.; Duan, X. Ultrafine Jagged Platinum Nanowires Enable Ultrahigh Mass Activity for the Oxygen Reduction Reaction. *Science* **2016**, *354*, 1414−1419.
(62) Xia, B. Y.; Wu, H. B.; Wang, X.; Lou, X. W. Highly Concave Platinum Nanoframes with High-Index Facets and Enhanced Electrocatalytic Properties. *Angew. Chem., Int. Ed.* **2013**, *52*, 12337−12340.
(63) Wang, J. X.; Markovic, N. M.; Adzic, R. R. Kinetic Analysis of Oxygen Reduction on Pt (111) in Acid Solutions: Intrinsic Kinetic Parameters and Anion Adsorption Effects. *J. Phys. Chem. B* **2004**, *108*, 4127−4133.
(64) Morozan, A.; Jousselme, B.; Palacin, S. Low-Platinum and Platinum-Free Catalysts for the Oxygen Reduction Reaction at Fuel Cell Cathodes. *Energy Environ. Sci.* **2011**, *4*, 1238−1254.
(65) Coleman, E. J.; Chowdhury, M. H.; Co, A. C. Insights Into the Oxygen Reduction Reaction Activity of Pt/C and PtCu/C Catalysts. *ACS Catal.* **2015**, *5*, 1245−1253.
(66) Jung, N.; Yeonsun, S.; Jin, H. P.; Kee, S. N.; Pil, K.; Sung, J. Y. High-Performance $PtCu_x$@Pt Core-Shell Nanoparticles Decorated with Nanoporous Pt Surfaces for Oxygen Reduction Reaction. *Appl. Catal., B* **2016**, *196*, 199−206.
(67) Stamenkovic, V. R.; Mun, B. S.; Mayrhofer, K. J.; Ross, P. N.; Markovic, N. M. Effect of surface composition on electronic structure, stability, and electrocatalytic properties of Pt-transition metal alloys: Pt-skin versus Pt-skeleton surfaces. *J. Am. Chem. Soc.* **2006**, *128*, 8813−8819.
(68) Stamenkovic, V.; Mun, B. S.; Mayrhofer, K. J. J.; Ross, P. N.; Markovic, N. M.; Rossmeisl, J.; Greeley, J.; Nørskov, J. K. Changing the Activity of Electrocatalysts for Oxygen Reduction by Tuning the Surface Electronic Structure. *Angew. Chem.* **2006**, *118*, 2963−2967.
(69) Koh, S.; Strasser, P. Electrocatalysis on Bimetallic Surfaces: Modifying Catalytic Reactivity for Oxygen Reduction by Voltammetric Surface Dealloying. *J. Am. Chem. Soc.* **2007**, *129*, 12624−12625.
(70) Srivastava, R.; Mani, P.; Hahn, N.; Strasser, P. Efficient Oxygen Reduction Fuel Cell Electrocatalysis on Voltammetrically Dealloyed Pt-Cu-Co Nanoparticles. *Angew. Chem.* **2007**, *119*, 9146−9149.

DOI: 10.1021/acsaem.9b00205
ACS Appl. Energy Mater. 2019, 2, 2862−2869